Supplementary Information for

A Conformational Transition of the D'D3 Domain primes von Willebrand Factor for Multimerization

Sophia Gruber[a], Achim Löf[a], Adina Hausch[a], Fabian Kutzki[b], Res Jöhr[a], Tobias Obser[c], Gesa König[d], Reinhard Schneppenheim[d], Camilo Aponte-Santamaria[b], Frauke Gräter[b], Maria A. Brehm[e], Martin Benoit[a,1], and Jan Lipfert[a,1]

[a]Department of Physics and Center for NanoScience, LMU Munich, 80799 Munich, Germany
[b]Heidelberg Institute for Theoretical Studies and University of Heidelberg, 69118 Heidelberg, Germany
[c]Department of Dermatology and Venerology, University Medical Center Hamburg-Eppendorf, 20246 Hamburg, Germany
[d]Department of Pediatric Hematology and Oncology, University Medical Center Hamburg-Eppendorf, 20246 Hamburg, Germany
[e]Department of Digital Health Sciences and Biomedicine, School of Life Sciences, University of Siegen, 57076 Siegen, Germany

[1]Corresponding authors:
Jan Lipfert, Department of Physics and Center for NanoScience, LMU Munich, Amalienstrasse 54, 80799 Munich, Germany, Tel: +49 89 2180 2005, e-mail: jan.lipfert@lmu.de
and
Martin Benoit, Department of Physics and Center for NanoScience, LMU Munich, Amalienstrasse 54, 80799 Munich, Germany, Tel: +49 89 2180 3133, Fax: +49 89 2180 2050, e-mail: martin.benoit@physik.uni-muenchen.de

Content:

Supplementary Materials and Methods
Supplementary Tables 1 and 2
Supplementary Figures 1-7

Supplementary Materials and Methods

VWF Constructs

Dimeric VWF constructs were designed as hetero-bifunctional dimers, consisting of two different types of monomers possessing different N-terminal peptide tags. One monomer possessed a ybbR-tag, allowing for covalent conjugation of CoA-biotin. The second monomer was equipped with a strep-tag II for high-affinity purification, followed by a tobacco etch virus (TEV) protease cleavage site[1] and the N-terminal sortase motif[2] GG. The TEV site served two purposes: First, to remove the strep-tag after purification, to avoid interaction with streptavidin on the magnetic beads, and second, to expose the sortase motif GG, which must be located terminally for the sortase-mediated ligation to the ELP linker. In addition to full-length dimers, comprising all domains present in mature VWF, also several constructs with deletions of certain domains were investigated as controls: delD4, with a deletion of the full D4 assembly (D4N-TIL4, aa 1873-2255), delD'D3, with a deletion of the full D'D3 assembly (TIL'-E3, aa 764-1273), and delA1, with a deletion of the A1 domain (aa 1272-1462). Additionally, an "inverted" construct was expressed, which dimerized N-terminally. To produce such N-terminally, but not C-terminally linked dimers, monomers with mutation p.Cys2771Arg in the CK domain to impair C-terminal dimerization[3,4] and with C-terminal tags for site-specific protein attachment were expressed in the presence of the VWF propeptide (VWFpp) domains D1 and D2.

Hetero-bifunctional dimers were obtained by co-transfection of HEK-293 cells with two different plasmids so that the two different types of monomers were co-expressed. Multimerization was obstructed by deleting the VWF pro-peptide sequence (domains D1 and D2, aa 26-763). N-terminal tags were inserted after the required N-terminal signal peptide (aa 1-25). Plasmid construction, transfection of HEK-293 cells and protein expression were performed as described in detail in Müller *et al.*[5]. In brief, $2 \cdot 10^6$ HEK-293 cells (DSMZ, Germany) were transfected in Dulbecco's modified Eagle's medium (Life Technologies) containing 10 % fetal bovine serum (Life Technologies), 2 µg of each of the two plasmids, and 15 µl Lipofectamine 2000 (Life Technologies).

24 h after transfection, cells were transferred into selection medium containing 500 µg/ml G418 (Invivogen) and 250 µg/ml Hygromycin B (Invivogen). After 2–3 weeks, the polyclonal cell culture was seeded for expression. After 72 h of cell growth, the medium was exchanged against OPTIPRO serum-free medium (Life Technologies) for serum-free collection of secreted recombinant VWF. The culture supernatant was collected after 72 h and concentrated using Amicon Ultra-15 MWCO 100 kDa (Merck Millipore).

All dimeric constructs were purified via a HiTrap StrepTrap affinity chromatography column (GE Healthcare) using the AEKTA Explorer system (GE Healthcare). As running buffer, 20mM Hepes, 150mM NaCl, 1mM $MgCl_2$, 1mM $CaCl_2$, pH 7.4, was used. Elution buffer additionally contained 2.5mM d-desthiobiotin. Eluted VWF constructs were buffer exchanged (to the running buffer) and concentrated by centrifuge filtration using Amicon UltraMWCO 100 kDa (Merck Millipore). After 5 washing steps with 500 µl of running buffer, the volume was decreased to ≈ 100 µl before inverting the filter and harvesting the protein.

Equilibrium Molecular Dynamics (MD) Simulations

The crystal-structure of the D'D3 domain served as the structural basis for the subsequent equilibrium simulations[6] (PDB ID 6N29). It contains 15 histidine residues and 478 residues in total. We set up two different configurations, one representing an environment at neutral pH and one simulating more acidic conditions by protonating all histidines. 10 different replicas were simulated for each case, solvated in a cubic box with ~75,000 explicit water molecules, 0.15 mol/l Na-Cl and two Ca^{2+} ions. To guarantee a net neutral charge of the system, excess ions were introduced. A steepest descent energy minimisation was performed (with an force tolerance of 1000 kJ/mol/nm) and subsequently an NPT solvent equilibration of 1 ns length was conducted with position restraints applied to the heavy atoms of the protein structure (elastic constant of 1000 kJ/mol/nm in each spatial dimension). Following that, position restraints were removed and the main production runs were conducted, generating between 100 to 400 ns for each replica. The LINCS algorithm was used to constrain protein bonds involving hydrogens[7] and the SETTLE algorithm[8] to constrain both angular and bond vibrations of the water (TIP3P[9]), enabling a 2 fs time step to propagate the leap-frog algorithm[10]. The first 20 ns of every run were discarded for the purpose of further equilibration, resulting in a total of at least 4.5 µs of cumulative MD simulation time for further analysis. See simulation parameters in Supplementary Table 2.

Force-Probe MD Simulation

Random configurations from the equilibrium runs were taken to set up three sets of constant velocity pulling simulations. Pulling rates were chosen to be 0.2 m/s, 0.1 m/s and 0.025 m/s. A cubic box of dimensions 60 nm x 12 nm x 12 nm was simulated, big enough to allow for unfolding along the x-axis. This box was filled with ~290,000 explicit water molecules, 0.15 mol/l Na-Cl, two Ca^{2+} ions and excess ions to guarantee a net neutral charge. An identical equilibration procedure and simulation parameters were used as in the equilibrium MD simulations (see Supplementary Table 2). Harmonic forces were applied to the N- (residue 1) and C-termini (residue 478) of the D'D3 domain in opposite directions. Simulations were continued until full elongation of the entire D'D3 structure was observed, resulting in 100 ns of simulation time per replica for a pulling rate of 0.2 m/s, 200 ns for 0.1 m/s, and 650-750 ns for 0.025 m/s. 10 simulation replicas were obtained for each histidine protonation state and pulling velocity (60 replicas in total) for a cumulative simulation time of 20 µs.

Simulation Analysis: Histdine Contacts from Equilibrium MD Simulations

We calculated the average number of histidine-domain contacts (inter-atomic distance <0.35 nm) by summing up the absolute number of such contacts between histidines in the D3 domain and residues in domain X and the absolute number of contacts between histidines in domain X and residues in D3, with X being TIL' (residues 1-64), E' (resdiues 65-100), C8-3 (residues 275-364), Til3 (residues 365-433), and E3 (residues 434-478) Contacts were computed for both protonation cases (i.e. at different pH levels) and averages taken over all frames. The standard error on the mean (SEM) is calculated from the standard deviation between individual time frames and the degree of auto-correlation number of effective degrees of freedom estimated by Equation 12, below. To check if averages in histidine-domain contacts differed between pH states, p-values were estimated with a *t*-test, taking the

effective degrees of freedom (see Equation 12 below), the mean and the standard error on the mean (SEM) as inputs.

Simulation Analysis: Normalised Elongation Plots for Pulling Simulations

To reduce the thermal noise in the data, all information from the force probe simulation trajectories were subjected to a Gaussian smoothing process. At incremental time steps of 0.1 ns, the average for that time was calculated by a normal distributed weight-function with sigma=0.2 ns for a pulling velocity of v=0.2 m/s, sigma=0.4 ns for v=0.1 m/s and sigma=1.6 ns for v=0.025 m/s. To quantify the degree of protein unfolding during force probe simulations, contact estimates were calculated for sub-domain interfaces on the basis of the absolute number of inter-atomic contacts Con[<0.5nm]. For the purpose of normalisation the interface between two sub-domains was considered intact (value R_{con}=1) at all times before the maximum number of contacts and completely nullified for all times after the minimum (R_{con}=0). For times t between maximum and minimum, the following normalisation formula was employed to estimate the degree of contact (Equation 11)

$$R_{con}(t) = \frac{Con(t) - Con_{av}(0, t_{max})}{Con_{av}(0, t_{max}) - Con_{av}(t_{min}, t_{end})} \tag{11}$$

with $Con_{av}(0,t_{max})$ the average number of inter-atomic contacts for times with completely intact interface and $Con_{av}(t_{min},t_{end,\infty})$ the average number of contacts for times where the sub-domains are completely detached. $R_{con}(t)$ was determined for all cases and replicas and subsequently transformed into a function of the distance increment during the pulling process $R_{con}(t) \rightarrow R_{con}(x)$. The average of $R_{con}(x)$ was calculated on the basis of the ten replicas for each protonation case and each pulling velocity.

Simulation Analysis: Rupture Distances and Forces

The force peak prior to the rupture event as well as the exact rupture distance (measured as an increment between protein length at the start of the simulation and at times t) were extracted from the simulations. As time of rupture, we considered the first passage of R_{con}<0.1, see Equation 11. *p*-values for regression line parameters were estimated by bootstrapping the posterior probability distribution of these parameters under the assumption that for each combination of pH case and pulling velocity, the 10 rupture forces and distances (1 from each replica) are *t*-distributed around the estimated mean.

Simulation Analysis: p-Values and Number of Uncorrelated Data Points

To extract correct error estimates for quantities calculated on the basis of MD time series, we took the degree of auto-correlation into account, transforming the total number of data points *n* into an effective number of statistically independent values n_{eff}:

$$n_{eff} = \frac{n}{1 + 2\sum_{k=1}^{n_c} (1 - \frac{k}{n}) r_k} \tag{12}$$

with r_k the auto-correlation function[11,12] estimated from the data and n_c the number of time frames until first zero transition of r_k. p-values could subsequently be estimated on the basis of a t-test using n_{eff} as the number of independent samples.

MT Instrument

MT experiments were performed on a previously described custom setup[13,14]. The setup employs a pair of permanent magnets (5×5×5 mm^3 each; W-05-N50-G, Supermagnete, Switzerland) in vertical configuration[15]. The distance between magnets and flow cell (and, thus, the force) is controlled by a DC-motor (M-126.PD2; PI Physikinstrumente, Germany). An LED (69647, Lumitronix LED Technik GmbH, Germany) is used for illumination. A 40x oil immersion objective (UPLFLN 40x, Olympus, Japan) and a CMOS sensor camera with 4096×3072 pixels (12M Falcon2, Teledyne Dalsa, Canada) allow to image a large field of view of approximately 440 × 330 μm^2 at a frame rate of 58 Hz. Images are transferred to a frame grabber (PCIe 1433; National Instruments, Austin, TX) and analyzed with a LabView-based open-source tracking software[16]. The bead tracking accuracy of the setup is ≈ 0.6 nm in (x, y) and ≈ 1.5 nm in z direction. For creating the look-up table required for tracking the bead positions in z, the objective is mounted on a piezo stage (Pifoc P-726.1CD, PI Physikinstrumente). Force calibration was conducted as described by te Velthuis *et al.*[17] based on the transverse fluctuations of long DNA tethers. Importantly, for the small extension changes on the length scales of our protein tethers, the force stays essentially constant[14], with the relative change in force due to tether stretching or protein unfolding being $< 10^{-4}$. Force deviations due to magnetic field inhomogeneities across the full range of the field of view are < 3%. The largest source of force uncertainty is the bead-to-bead variation, which is on the order of ≤ 10% for the beads used in this study[14,15,18,19].

Single Molecule MT Measurements

Preparation of flow cells was performed as described[14]. In brief, aminosilanized glass slides were functionalized with elastin-like polypeptide (ELP) linkers[20], possessing a single cysteine at their N terminus as well as a C-terminal Sortase motif, via a small-molecule crosslinker with a thiol-reactive maleimide group [sulfosuccinimidyl 4-(N-maleimidomethyl)cyclohexane-1-carboxylate; Sulfo-SMCC, Thermo Fisher Scientific]. Flow cells were then assembled from an ELP-functionalized slide as bottom and a non-functionalized glass slide with two small holes for inlet and outlet as top, with a layer of cut-out parafilm (Pechiney Plastic Packaging Inc., Chicago, IL) in between to form a channel. Flow cells were incubated with 1 % casein solution (Sigma-Aldrich) for 1 h and flushed with 1 ml (approximately 20 flowcell volumes) of buffer pH 7.4, near physiological (Supplementary Table 1).

CoA-biotin (New England Biolabs) was coupled to the ybbR-tag of the VWF-dimer constructs in a bulk reaction in the presence of 5 μM sfp phosphopantetheinyl transferase[21] and 10 mM $MgCl_2$ at 37 °C for 60 min. Afterwards, VWF dimers were diluted to a final concentration of approximately 20 nM in pH 7.4, near physiological buffer (Supplementary Table 1), and incubated in the flow cell in the presence of 2 μM evolved pentamutant Sortase A[22,23] for 30 min. Subsequently, the flow cell was flushed with 1 ml of measurement buffer (pH 7.4, near physiological buffer with 0.1 % Tween-20 (Supplementary Table 1)). Finally,

beads functionalized with streptavidin (Dynabeads M-270, Invitrogen) were incubated in the flow cell for 60 s, and unbound beads were flushed out with 1 ml of measurement buffer.
At the beginning of each measurement, the tethered beads were subjected to two 5-min intervals of a constant force of 11 pN to allow for identification of specific, single-tethered beads by the characteristic unfolding of the two A2 domains[14] (Fig. 2A, green inset). Only beads that showed two A2 unfoldings were analyzed further. After 30 s at a low resting force of 0.5 pN, beads were subjected to a forceramp starting at 12 pN and going down to 6 pN in steps of 0.3 pN, with each plateau of constant force lasting for 5 minutes. All measurements were performed at room temperature ≈ 22 °C). For testing the transitions under different buffer conditions, buffer was exchanged and the same measurement protocol was repeated. Buffer composition of different buffers are listed in Supplementary Table 1.
To test the influence of Factor VIII, we used a haemophilia A drug – Advate 500 I.E. (Baxter AG, Wien, Austria) – containing octocog alfa, recombinant human factor VIII. The recombinant factor FVIII has post-translational modifications similar to plasma-derived molecules, according to the EMEA documentation of the product (https://www.ema.europa.eu/en/medicines/human/EPAR/advate). After diluting the powder according to the manufacturers instructions, we filtered the recombinant FVIII, exchanged the buffer to our measurement buffer with pH 7.4, and increased the concentration by centrifuge filtration using Amicon UltraMWCO 100 kDa (Merck Millipore): After 5 washing steps with the measurement buffer, we decreased the volume to ≈ 90 µl before harvesting F-VIII by filter inversion. This resulted in a FVIII concentration of 0.642 µM. The ≈ 90 µl were inserted into the flowcell and incubated for 30 min before repeating the same measurement protocol described above.

Data Analysis

Data analysis was performed with custom MATLAB scripts. Specific VWF dimer tethers were selected on the basis of the two A2 fingerprint unfolding events, characterized previously[5,14]. Extension vs. time traces were subjected to a tether-specific smoothing with a moving average filter. The number of frames used for the smoothing was determined based on the distance of the states and the Allan Deviation (AD) of the tether extension fluctuation (see Supplementary Figure 2). The distance between the states Δz was determined from fitting a double or triple Gaussian function to the histogram of the extension in the lowest constant force plateau exhibiting a population in all two or three-states, respectively and evaluating the distance between the peaks, as shown in Supplementary Figure 2B to the left (1.)). The AD was calculated from a 30 second fragment of the trace at the lowest constant force plateau exhibiting no transitions and fit with a theoretical model of an overdamped bead (Supplementary Figure 2B middle (2.))). The AD is defined as

$$\sigma_\theta(\tau) = \sqrt{\frac{1}{2} < (z_{i+1} - z_i)^2 >} \tag{13}$$

where z_i is the mean of the measurement interval of length τ. The angle bracket denotes the arithmetic mean over all measurement intervals. In other words, the AD is one-half of the averaged square distance between the means of neighbouring intervals[24–26]. Intuitively, it gives a measure of the spatial resolution after averaging over a time interval τ. Using the criterion that the deviation should be at least four times smaller than the evaluated distance

Δz, a smoothing factor for each trace can be determined by multiplication of the averaging interval τ, where AD equals $\Delta z/4$, with the measurement frequency. This smoothing factor – typically in the range of 8 to 13 frames – is applied to the time extension-time trace before evaluation of the state-population and the dwell times in each force plateau.

Supplementary Tables and Figures

Name	Ingredients	Number of molecules
pH 7.4	20 mM Hepes, 150 mM NaCl, 1 mM $CaCl_2$, 1 mM $MgCl_2$	33
pH 7.4 + EDTA	20 mM Hepes, 150 mM NaCl, 10 mM EDTA	16
pH 6.2	20 mM BisTris, 150 mM NaCl, 1 mM $CaCl_2$, 1 mM $MgCl_2$	11
pH 5.5	20 mM Na-Acetate, 150 mM NaCl, 1 mM $CaCl_2$, 1 mM $MgCl_2$	4
pH 7.4 + FVIII	20 mM Hepes, 150 mM NaCl, 1 mM $CaCl_2$, 1 mM $MgCl_2$ + 640 nM FVIII	5

Supplementary Table 1: Buffers used for MT measurements. The pH of buffers was adjusted with HCl and NaOH. For the measurement, buffers were supplemented with 0.1 % Tween-20 to reduce unspecific interactions of beads.

Parameter Class	Parameter	Equilibrium	Const. v force-probe
System	MD Code	GROMACS-2018/20 [27]	GROMACS-2018/20
Integration	Integrator Cut-Off-Scheme PBC Force Field dt	MD Verlet [28] XYZ AMBER99sb-ildnp-start [29,30] 2 fs	MD Verlet XYZ AMBER99sb-ildnp-star 2 fs
Non-bonded interactions	Coulomb Electrostat. Coulomb Modifier Coulomb Radius vdW Interaction vdW Modifier vdW Switch Radius vdW Radius	PME [31,32] Potential-Shift-Verlet 1.1 nm Cutoff Force-Switch 1.0 nm 1.1 nm	PME Potential-Shift-Verlet 1.1 nm Cutoff Force-Switch 1.0 nm 1.1 nm
Thermo-/Barostat	Temp. Coupling Pressure Coupling Temp. update time Ref. Temperature Pressure update time Temp. Groups	V-Rescale [33] Parinello-Rahman [34] 0.5 ps 300 K 5 ps Protein, Non-Protein	V-Rescale Parinello-Rahman 0.5 ps 300 K 5 ps Protein, Non-Protein
Pulling	Pulling Geometry Pulling Rate Spring Constant	- - -	Direction 0.2 | 0.1 | 0.025 m/s 500 kJ/mol/nm^2

Supplementary Table 2: MD parameters for D'D3 (force probe) molecular dynamics simulations.

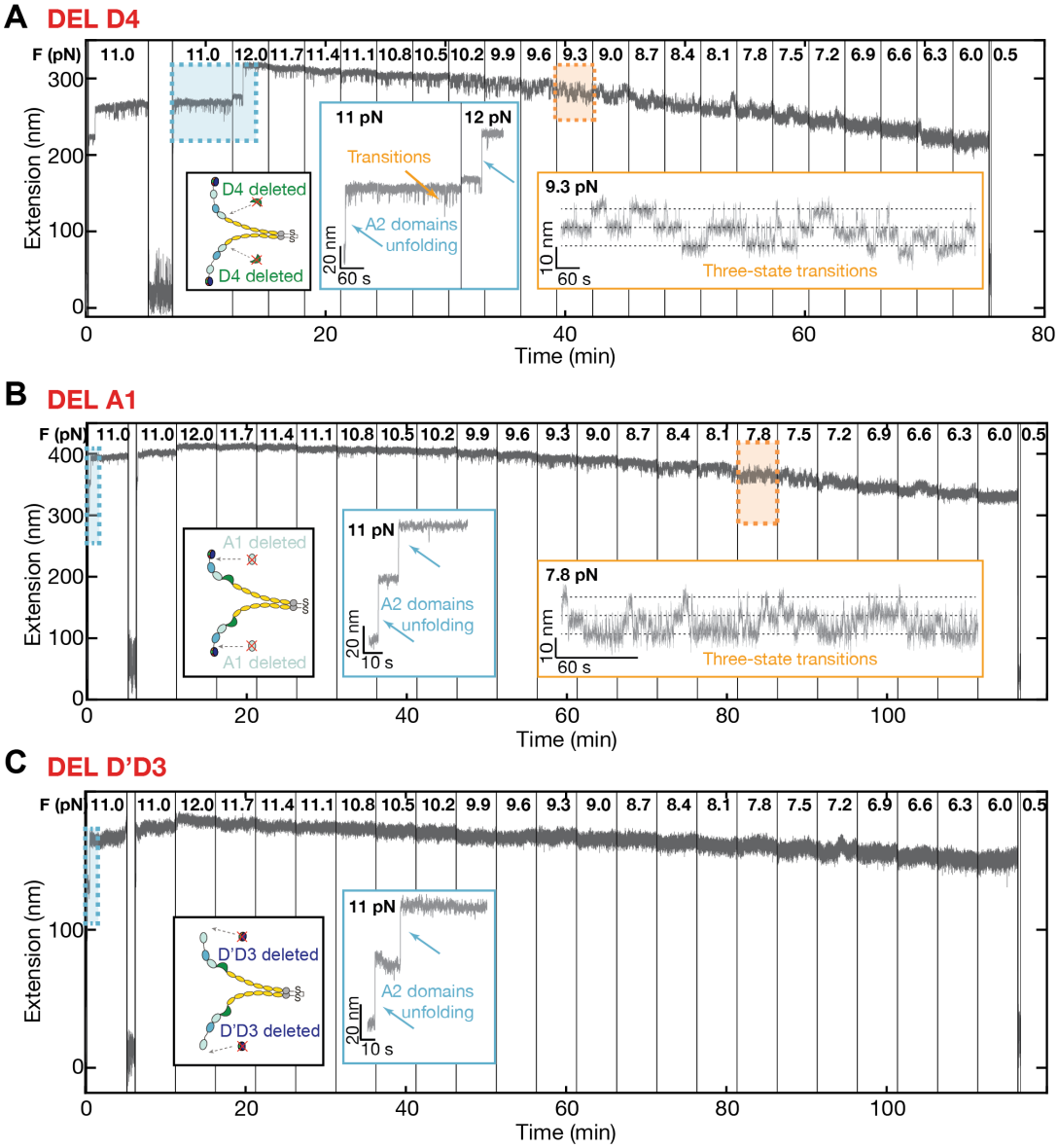

Supplementary Figure 1. Control measurements with domain deletions to assign the transitions to the D'D3 domain. Individual domains were deleted to verify the origin of the transitions in the D'D3 domain. Apart from deleted domains, constructs possessed the same tags and were objected to the same force protocol as the wild type. **A** Heterodimer with D4 domain deletions (schematic of construct shown as inset (black frame)). Molecules with D4 domain deletions show A2 domain unfolding events (inset with blue frame) and three-state transitions (inset with orange frame), proving transitions to be independent of the D4 domain. Notably, transitions also appear in between the two A2 unfolding events, suggesting that transitions are also independent of the A2 domain. **B** Heterodimer with A1 domain deletions (schematic of construct shown as inset (black frame)). Molecules with A1 domain deletions show A2 domain unfolding events (inset with blue frame) and three-state transitions (inset with orange frame), proving transitions to be independent of the A1 domain. **C** Heterodimer with D'D3 domain deletions (schematic of construct shown as inset (black frame)). Constructs with D'D3 domain deletions show A2 domain unfolding events, but no transitions. This was checked for > 40 molecules. The absence of transitions in this deletion construct strongly suggests that transitions originate in the D'D3 domain.

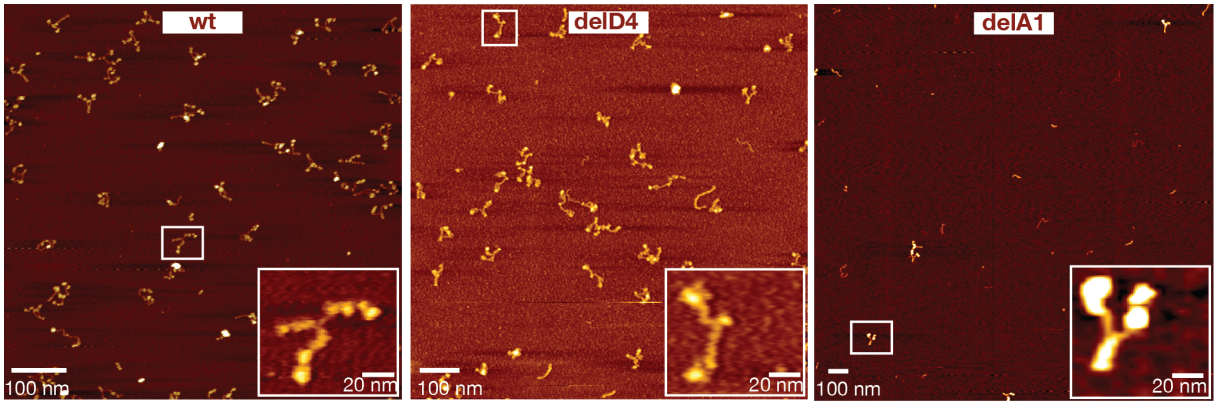

Supplementary Figure 2. AFM images of VWF deletion constructs. AFM images of wildtype, delD4 (D4 domain deleted), and delA1 (A1 domain deleted) VWF constructs. These are the same constructs used for control measurements (Figure 3). Images were recorded in tapping mode in air using an MFP-3D AFM (Asylum Research) after deposition of VWF constructs on freshly cleaved mica coated with poly-L-lysine[5,35]. The images reveal that dimerization is unaffected by the deletion of the individual domains. Different surface densities can be rationalized through different concentrations of the three constructs.

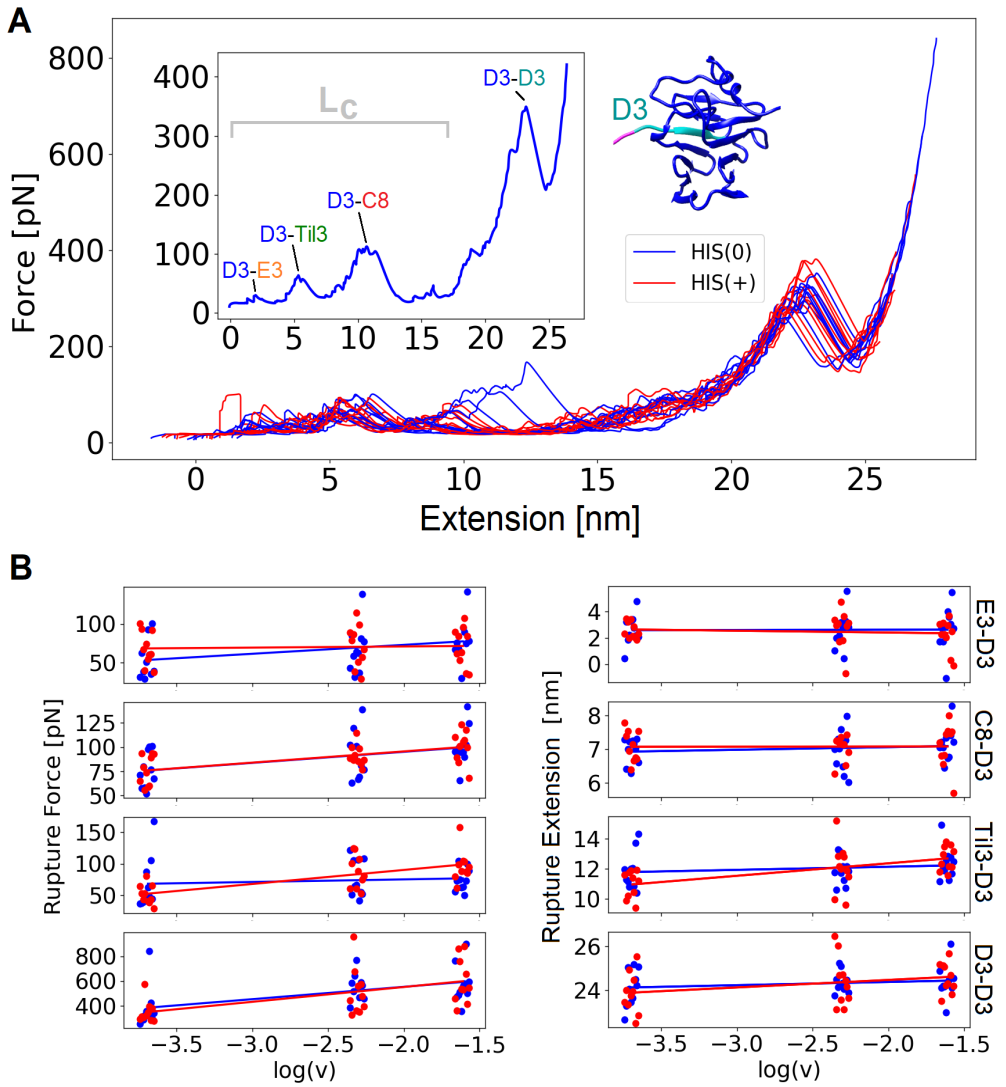

Supplementary Figure 3. Force-probe molecular dynamics simulations of the VWF D'D3 domain. A Force-extension curves from force-probe MD simulations pulling the termini away from each other at a pulling velocity of 0.025 m/s. Simulations were conducted both with the histidines uncharged (HIS(0), blue) or protonated (HIS(+), red). 10 simulations were carried out for each protonation state. The inset shows a single replica indicating the major rupture events. The contour length L_C change upon interface opening was estimated as the extension increment from the beginning of the simulation to the point where the E3, TIL3, C8-3 domains are peeled off from the VWD3 domain and where the force ramps up to the average value of the highest previous force peak (length indicated by the grey bracket). The last rupture event at around 24 nm extension is associated with the unfolding of a beta-strand (show in cyan in the inset) from the D3 sub-domain (shown in blue). **B** Rupture Forces (left) and extensions (right) are shown for the four main unfolding events (E3-D3, C8-D3, TIL3-D3, D3-D3) and both histidine protonation states (unprotonated: blue, and protonated: red) as a function of the pulling velocities, shown logarithmically on the x-axis with v measured in m/s. Lines are from a linear regression. Regression line parameters are very similar for protonated and unprotonated histidines for all domains except for C8-D3, where the slope and y-intersection noticeably differ, although not in a statistically significant way.

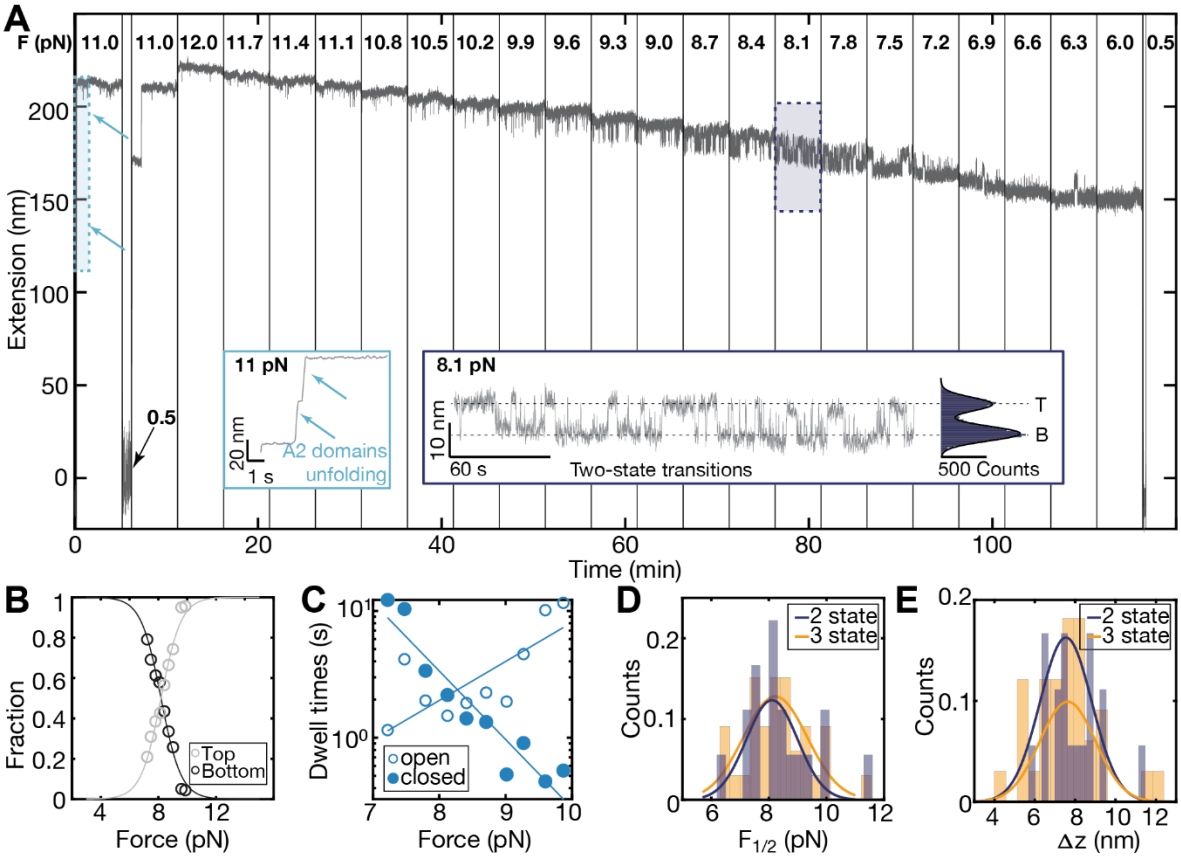

Supplementary Figure 4. Exemplary dwell time evaluation for an extension-time trace at constant force. A Short segment of a extension-time trace measured for a wild type D'D3 domain VWF dimer exhibiting three-state transitions at a force of 8.4 pN. Raw data are filtered with an 11-frame moving average (which is the smoothing factor determined according to Supplementary Figure 2 for this molecule). The green horizontal line is the threshold between the bottom state (B) and the middle state (M) and the blue horizontal line is the threshold between the middle state (M) and the top state (T); yellow squares indicate the first data point after crossing the threshold from below, i.e. transition from B to M or from M to T; red squares indicate the first data point after crossing the threshold from above, i.e. transition from T to M or M to B. **B** Time trace derived from the analysis shown in panel A, indicating the current state of D3 domains with "T" corresponding to both domains opened, "M" corresponding to one domain open and one domain closed and "B" corresponding to both domains closed. The time between the transitions between "B" and "M" and "M" and "T" correspond to the dwell times. To obtain pseudo dwell time distributions of the individual domains, dwell times in the bottom state were collected together with half of the dwell times in the middle state for a distribution of τ_{closed} and dwell times in the top state were collected with half of the dwell times in the middle state for a distribution of τ_{open}. **C, D** Histograms of pseudo dwell time distribution in the closed state (**C**) and the open state (**D**) obtained from the analysis shown in panels A and B. The pseudo dwell times are well described by single exponential fits, shown as solid orange line. Insets show the mean dwell time.

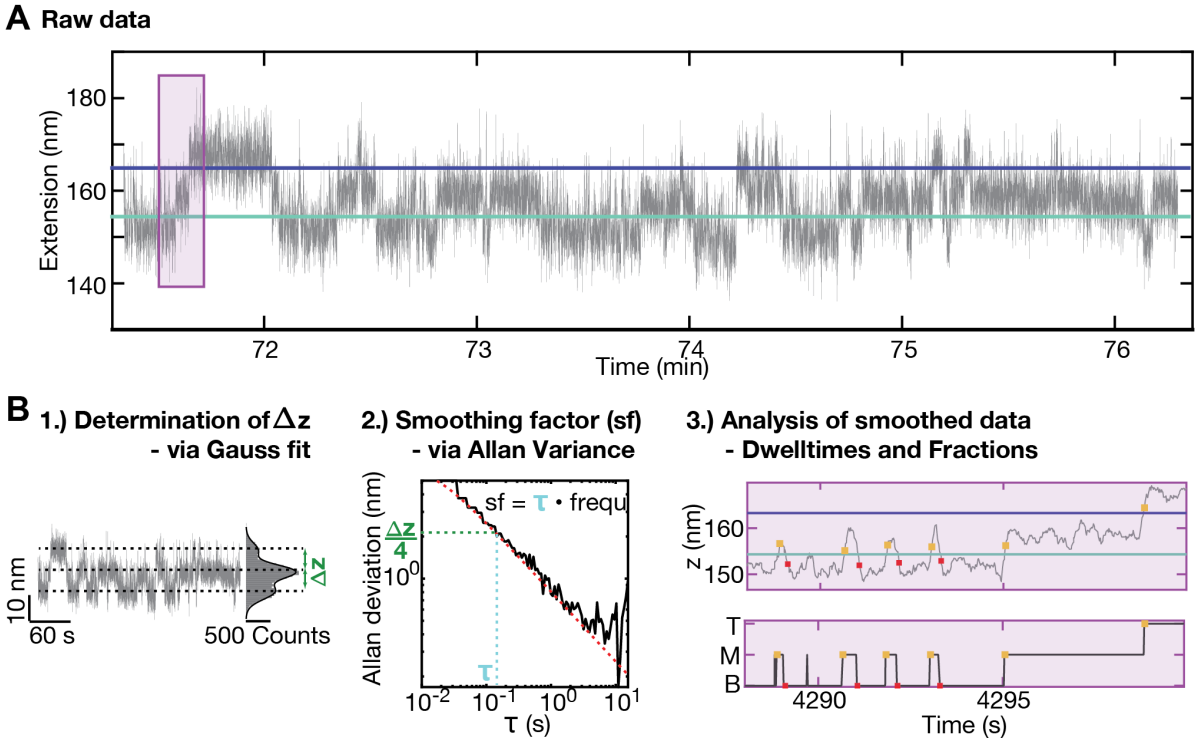

Supplementary Figure 5. Analysis procedure of extension-time traces exhibiting three-state transitions. A Raw data of an extension-time trace, recorded at 58 Hz in one constant force plateau. Thresholds separating bottom (B), middle (M), and top (T) states are shown as green and blue solid lines. Noise of the trace induces transitions over the thresholds in addition to transitions caused by domain opening and closing. The purple box indicates exemplary segment of the trace analyzed in panel B3 after the analysis. **B** Procedure to determine smoothing factor for dwell time analysis. In a first step, a three-term Gaussian is fit to the extension histogram and the distance between the fitted peaks indicates the Δz that needs to be resolved for dwell time analysis. Dashed lines indicate the T, M, and B state. Secondly, the Allan deviation for a 30 second time interval at the lowest force plateau for this molecule is calculated (solid black line, according to Equation 13) and fit with a theoretical model of the Allan deviation (red dashed line). The Allan deviation is defined as the square root of one-half of the averaged square distance between the means of neighbouring intervals of length τ[24]. Intuitively, it gives a measure of the spatial resolution after averaging over a time interval τ. Using the criterion that the deviation should be four times smaller than the distance Δz (green dashed line), a smoothing factor for each trace is determined depending on its noise level (blue dashed line). This smoothing factor is applied to the trace before analysing dwell times and fractions in a third step (right panel). Yellow squares indicate the first data point after crossing the threshold from below, i.e. transition from B to M or from M to T; red squares indicate the first data point after crossing the threshold from above, i.e. transition from T to M or M to B.

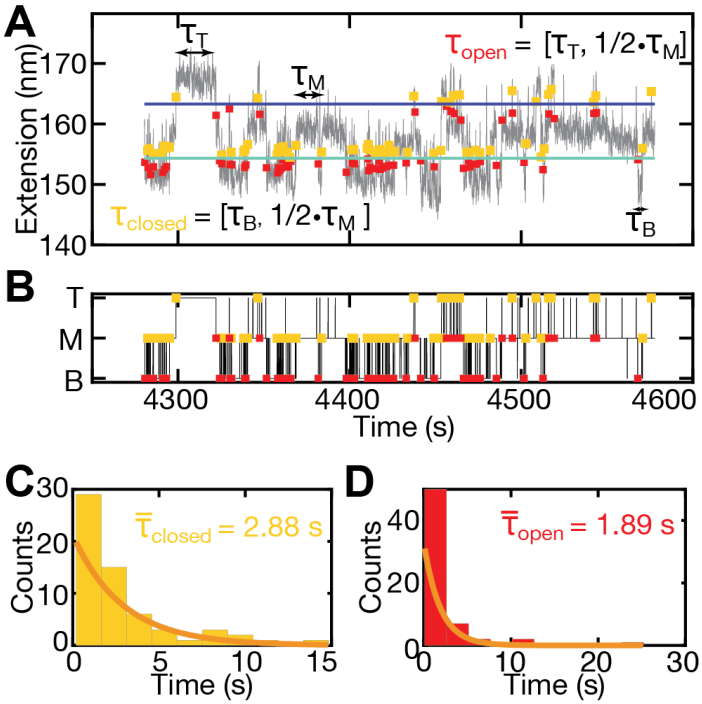

Supplementary Figure 6. Exemplary dwell time evaluation for an extension-time trace at constant force. A Short segment of a extension-time trace measured for a wild type D'D3 domain VWF dimer exhibiting three-state transitions at a force of 8.4 pN. Raw data are filtered with an 11-frame moving average (which is the smoothing factor determined according to Supplementary Figure 2 for this molecule). The green horizontal line is the threshold between the bottom state (B) and the middle state (M) and the blue horizontal line is the threshold between the middle state (M) and the top state (T); yellow squares indicate the first data point after crossing the threshold from below, i.e. transition from B to M or from M to T; red squares indicate the first data point after crossing the threshold from above, i.e. transition from T to M or M to B. **B** Time trace derived from the analysis shown in panel A, indicating the current state of D3 domains with "T" corresponding to both domains opened, "M" corresponding to one domain open and one domain closed and "B" corresponding to both domains closed. The time between the transitions between "B" and "M" and "M" and "T" correspond to the dwell times. To obtain pseudo dwell time distributions of the individual domains, dwell times in the bottom state were collected together with half of the dwell times in the middle state for a distribution of τ_{closed} and dwell times in the top state were collected with half of the dwell times in the middle state for a distribution of τ_{open}. **C, D** Histograms of pseudo dwell time distribution in the closed state (**C**) and the open state (**D**) obtained from the analysis shown in panels A and B. The pseudo dwell times are well described by single exponential fits, shown as solid orange line. Insets show the mean dwell time.

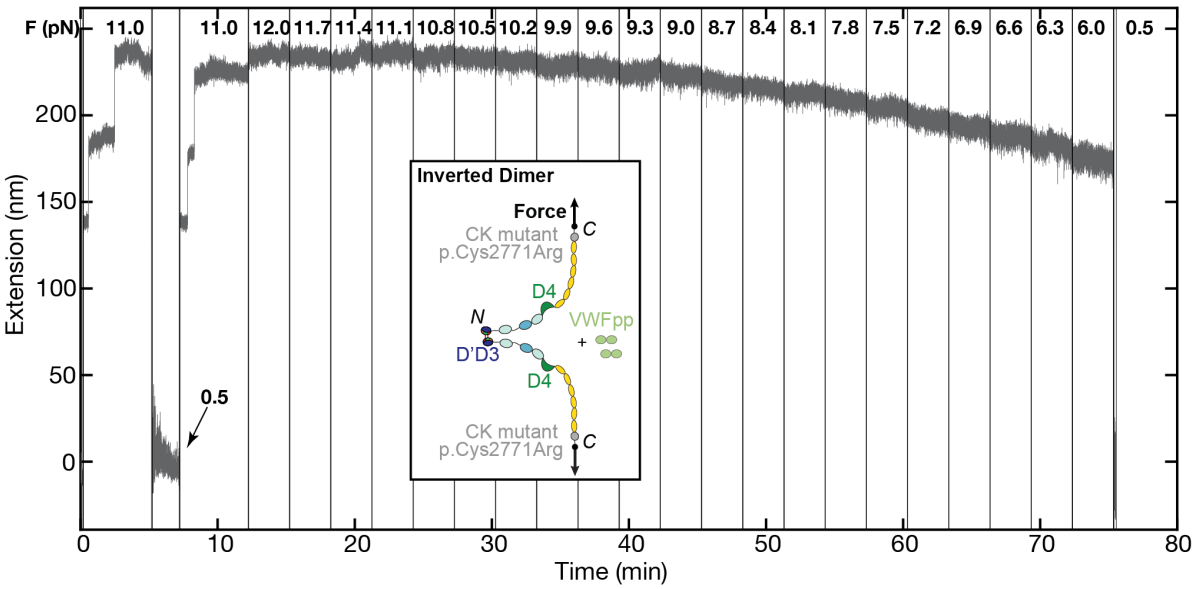

Supplementary Figure 7. Physiological force-loading of an inverted dimer. Extension-time traces under the same force ramp protocol that was used to analyze the two- and three-state transitions with an inverted dimer (schematic of construct shown as inset). In this conformation, force propagates through the D'D3 domain as through VWF that is multimerized by cysteine linkage in the D'D3 domains (see Figure 1). Extension was smoothed with a 5-frame moving average filter. In total, >40 inverted molecules with two A2 unfolding events were screened for transitions, but none showed any.

Supplementary References

1. Phan J, Zdanov A, Evdokimov AG, et al. Structural basis for the substrate specificity of tobacco etch virus protease. *J. Biol. Chem.* 2002;277(52):50564–50572.
2. Theile CS, Witte MD, Blom AEM, et al. Site-specific N-terminal labeling of proteins using sortase-mediated reactions. *Nat. Protoc.* 2013;8(9):1800–1807.
3. Brehm MA, Huck V, Aponte-Santamaría C, et al. von Willebrand disease type 2A phenotypes IIC, IID and IIE: A day in the life of shear-stressed mutant von Willebrand factor. *Thromb. Haemost.* 2014;112(1):96–108.
4. Lippok S, Kolšek K, Löf A, et al. Von Willebrand factor is dimerized by protein disulfide isomerase. *Blood*. 2016;127(9):1183–1191.
5. Müller JP, Mielke S, Löf A, et al. Force sensing by the vascular protein von Willebrand factor is tuned by a strong intermonomer interaction. *Proc. Natl. Acad. Sci. U. S. A.* 2016;113(5):1208–1213.
6. Dong X, Leksa NC, Chhabra ES, et al. The von Willebrand factor D'D3 assembly and structural principles for factor VIII binding and concatemer biogenesis. *Blood*. 2019;133(14):1523–1533.
7. Hess, Berk and Bekker, Henk and Berendsen, Herman JC and Fraaije JG. LINCS: a linear constraint solver for molecular simulations. *J. Comput. Chem.* 1997;18(12):1463--1472.
8. Miyamoto S, Kollman PA. Settle: An analytical version of the SHAKE and RATTLE algorithm for rigid water models. *J. Comput. Chem.* 1992;13(8):952–962.
9. Mahoney MW, Jorgensen WL. A five-site model for liquid water and the reproduction of the density anomaly by rigid, nonpolarizable potential functions. *J. Chem. Phys.* 2000;112(20):8910–8922.
10. Hockney RW, Goel SP, Eastwood JW. Quiet high-resolution computer models of a plasma. *J. Comput. Phys.* 1974;14(2):148–158.
11. Zięba A. Effective number of observations and unbiased estimators of variance for autocorrelated data-an overview. *Metrol. Meas. Syst.* 2010;(1):.
12. Zięba A, Ramza P. Standard deviation of the mean of autocorrelated observations estimated with the use of the autocorrelation function estimated from the data. *Metrol. Meas. Syst.* 2011;18(4):529–542.
13. Walker PU, Vanderlinden W, Lipfert J. Dynamics and energy landscape of DNA plectoneme nucleation. *Phys. Rev. E*. 2018;98(4):42412.
14. Löf A, Walker PU, Sedlak SM, et al. Multiplexed protein force spectroscopy reveals equilibrium protein folding dynamics and the low-force response of von Willebrand factor. *Proc. Natl. Acad. Sci. U. S. A.* 2019;116(38):18798–18807.
15. Lipfert J, Hao X, Dekker NH. Quantitative modeling and optimization of magnetic tweezers. *Biophys. J.* 2009;96(12):5040–5049.
16. Cnossen JP, Dulin D, Dekker NH. An optimized software framework for real-time, high-throughput tracking of spherical beads. *Rev. Sci. Instrum.* 2014;85(10):103712.
17. Te Velthuis AJW, Kerssemakers JWJ, Lipfert J, Dekker NH. Quantitative guidelines for force calibration through spectral analysis of magnetic tweezers data. *Biophys. J.* 2010;99(4):1292–1302.
18. de Vlaminck I, Henighan T, van Loenhout MTJ, Burnham DR, Dekker C. Magnetic forces and dna mechanics in multiplexed magnetic tweezers. *PLoS One*. 2012;7(8):.
19. Ostrofet E, Papini FS, Dulin D. Correction-free force calibration for magnetic tweezers experiments. *Sci. Rep.* 2018;8(1):1–10.
20. Ott W, Nash MA, Jobst MA, et al. Elastin-like Polypeptide Linkers for Single-Molecule Force Spectroscopy. *ACS Nano*. 2017;11(6):6346–6354.
21. Yin J, Straight PD, McLoughlin SM, et al. Genetically encoded short peptide tag for versatile protein labeling by Sfp phosphopantetheinyl transferase. *Proc. Natl. Acad.*

Sci. U. S. A. 2005;102(44):15815–15820.
22. Chen I, Dorr BM, Liu DR. A general strategy for the evolution of bond-forming enzymes using yeast display. *Proc. Natl. Acad. Sci. U. S. A.* 2011;108(28):11399–11404.
23. Durner E, Ott W, Nash MA, Gaub HE. Post-Translational Sortase-Mediated Attachment of High-Strength Force Spectroscopy Handles. *ACS Omega*. 2017;2(6):3064–3069.
24. Allan DW. Statistics of Atomic Frequency Standards. *Proc. IEEE*. 1966;54(2):221–230.
25. Czerwinski F, Richardson AC, Oddershede LB. Quantifying Noise in Optical Tweezers by Allan Variance. *Opt. Express*. 2009;17(15):13255.
26. van Oene MM, Ha S, Jager T, et al. Quantifying the Precision of Single-Molecule Torque and Twist Measurements Using Allan Variance. *Biophys. J.* 2018;114(8):1970–1979.
27. Abraham MJ, Murtola T, Schulz R, et al. GROMACS: High performance molecular simulations through multi-level parallelism from laptops to supercomputers. *SoftwareX*. 2015;1:19–25.
28. Páll S, Hess B. A flexible algorithm for calculating pair interactions on SIMD architectures. *Comput. Phys. Commun.* 2013;184(12):2641–2650.
29. Lindorff□Larsen K, Piana S, Palmo K, et al. Improved side□chain torsion potentials for the Amber ff99SB protein force field. *Proteins Struct. Funct. Bioinforma.* 2010;78(8):1950–1958.
30. Aliev AE, Kulke M, Khaneja HS, et al. Motional timescale predictions by molecular dynamics simulations: case study using proline and hydroxyproline sidechain dynamics. *Proteins Struct. Funct. Bioinforma.* 2014;82(2):195–215.
31. Darden T, York D, Pedersen L. Particle mesh Ewald: An N·log(N) method for Ewald sums in large systems. *J. Chem. Phys.* 1993;98(12):10089–10092.
32. Essmann U, Perera L, Berkowitz ML, et al. A smooth particle mesh Ewald method. *J. Chem. Phys.* 1995;103(19):8577–8593.
33. Bussi G, Donadio D, Parrinello M. Canonical sampling through velocity rescaling. *J. Chem. Phys.* 2007;126(1):14101.
34. Parrinello M, Rahman A. Polymorphic transitions in single crystals: A new molecular dynamics method. *J. Appl. Phys.* 1981;52(12):7182–7190.
35. Müller JP, Löf A, Mielke S, et al. pH-Dependent Interactions in Dimers Govern the Mechanics and Structure of von Willebrand Factor. *Biophys. J.* 2016;111(2):312–322.